

Supplemental Information

Nano-spots Induced Break of Boron Chemical Inertness :

A New Route toward

Reversible Hydrogen Storage Applications

Martin Depardieu,^{1,3} Raphaël Janot,^{2*} Clément Sanchez,³ Hervé Deleuze,⁴
Christel Gervais,³ Marc Birot,⁴ Mathieu Morcrette² and Rénal Backov^{1*}

¹ Université de Bordeaux, Centre de Recherche Paul Pascal, UPR 8641 CNRS, 115 Avenue Albert Schweitzer, 33600 Pessac, France. Email : backov@crpp-bordeaux.cnrs.fr

² Laboratoire de Réactivité et Chimie des Solides, UMR 7314 CNRS, Université de Picardie Jules Verne, 33 Rue Saint Leu, 80039 Amiens, France. Email : raphael.janot@u-picardie.fr

³ Laboratoire de Chimie de la Matière Condensée de Paris, UMR 7574 CNRS, UPMC Université Paris 06, Collège de France, 11 Place Marcelin Berthelot, 75231 Paris, France.

⁴ Université de Bordeaux, Institut des Sciences Moléculaires, UMR 5255 CNRS, 351 cours de la Libération, 33405 Talence, France

The starting metal-free carbonaceous foams obtained from the use of Si(HIPE) as a hard template, are monolithic, bearing open macroporosity with a texture that resembles aggregated hollow spheres (Figure S1).

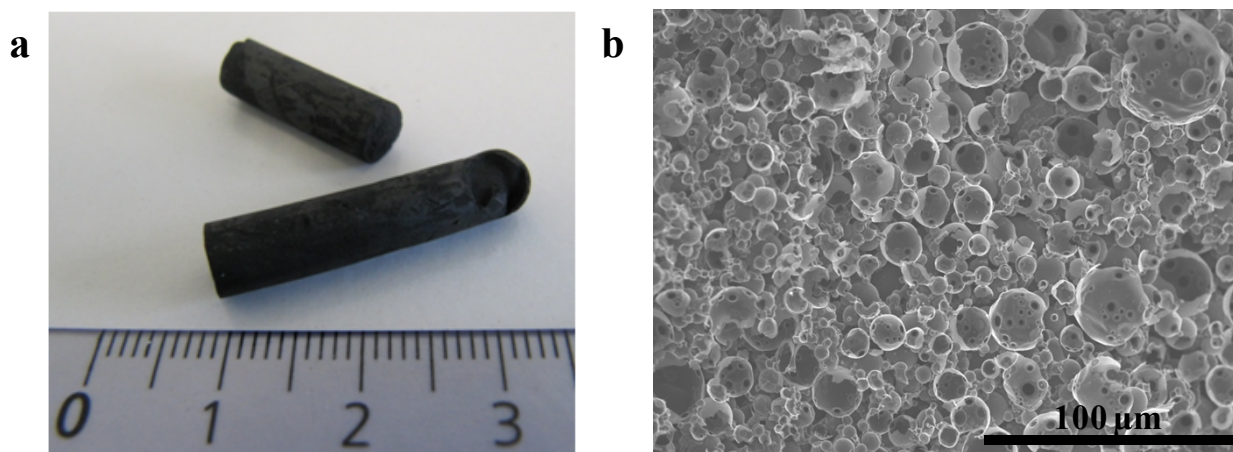


Figure S1. (a) Photograph showing the monolithic character of the foams. (b) SEM micrograph of the starting C-HIPE_(25HF) macrocellular carbonaceous foam.

After infiltration of the metallic salts and their reduction, the Pd and Au nanoparticles repartition can be appreciated at the macroscopic length scale by SEM using back-scattered electrons (Figure S2). The particles repartition is rather homogeneous from the exterior of the sample to its core. Some metallic nanoparticles aggregation is observed for both Pd and Au-containing samples.

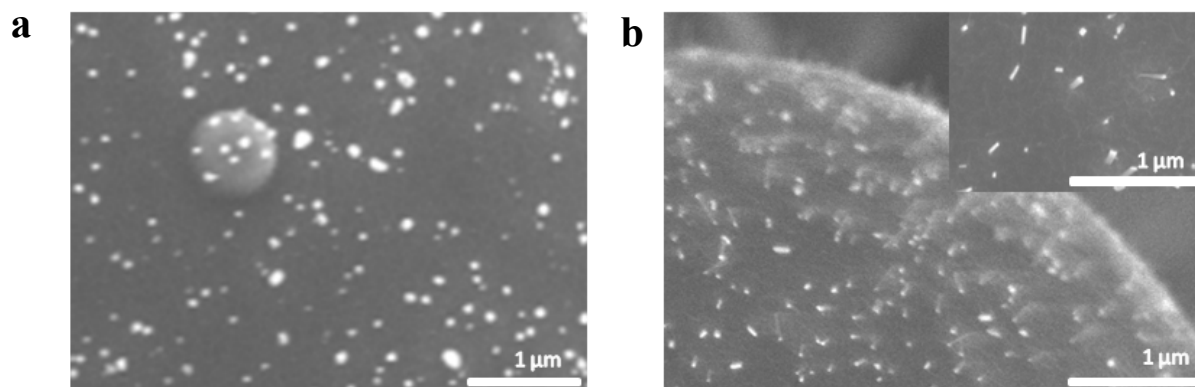


Figure S2. SEM micrographs using back-scattered electrons. (a) Pd@C-HIPE_(25HF) (b) Au@C-HIPE_(25HF). The shiny spots correspond to high electron diffusion region bearing materials with high electronic density, namely Au and Pd nanoparticles and their random distribution.

To characterize the Pd@C-HIPE_(25HF) and the Au@C-HIPE_(25HF) macrocellular foams at the macroscopic length scale, we have performed mercury porosimetry to establish their bulk and skeleton densities as well as the diameter distribution of the connecting windows of adjacent cells. We have to underline here that mercury porosimetry assesses only the diameters that minimize mercury infiltration; this is to say the windows that connect adjacent cells and not the cells themselves. The window diameters distributions are depicted within the Figure S3.

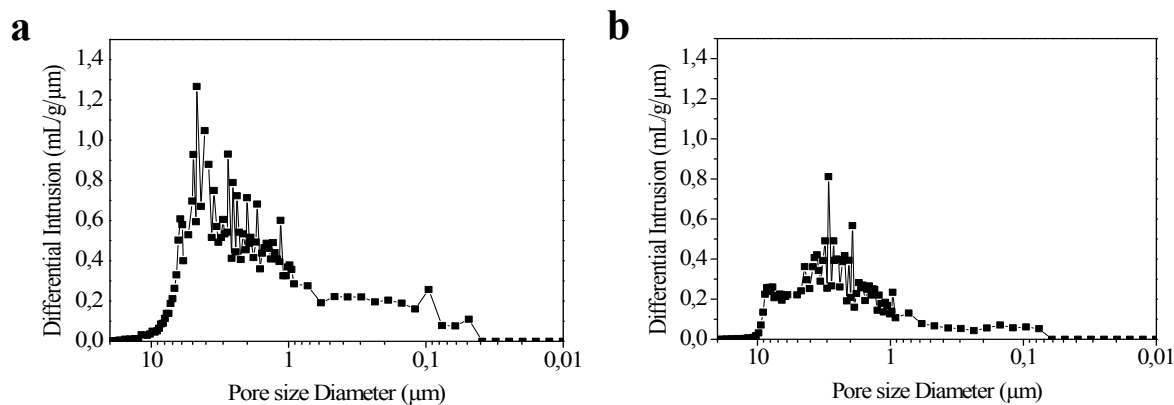


Figure S3. Windows pore sizes distribution obtained through Mercury porosimetry. (a) Pd@C-HIPE_(25HF) (b) Au@C-HIPE_(25HF).

As observed for the Si(HIPE) used as a hard template, the windows are polydisperse. This feature is induced by the aggregated hollow spheres aspect leading to the coexistence of internal and external cell junctions. We can notice that the superimposed bimodal values fall above 1 μm (external junctions) and below 100 nm (internal ones). Mercury porosimetry also provides information regarding the foams percentage of porosity, as well as bulk and skeleton densities: the results are summarized in the Table S1.

Table S1. Foams macroscopic characteristics extracted from mercury porosimetry.

Materials	Intrusion volume (cm^3/g)	Porosity (%)	Bulk density (g/cm^3)	Skeletal density (g/cm^3)
Pd@C-HIPE _(25HF)	4.51	78	0.17	0.81
Au@C-HIPE _(25HF)	3.25	74	0.23	0.90

The overall percentage of porosity falls completely within the range of carbonaceous foams previously obtained. The main difference emerges from the bulk and skeleton densities that are higher because now bearing metallic nanoparticles that increases the foams densities. The skeleton density is indeed a cooperative result between walls porosity and nanoparticles

load. For instance, the Au@C-HIPE_(25HF) sample possesses the highest skeleton density (Table S1) bearing the highest metallic nanoparticles weight percent. At the mesoscopic length scale nitrogen physisorption measurements have been made, results are shown in Figure S4.

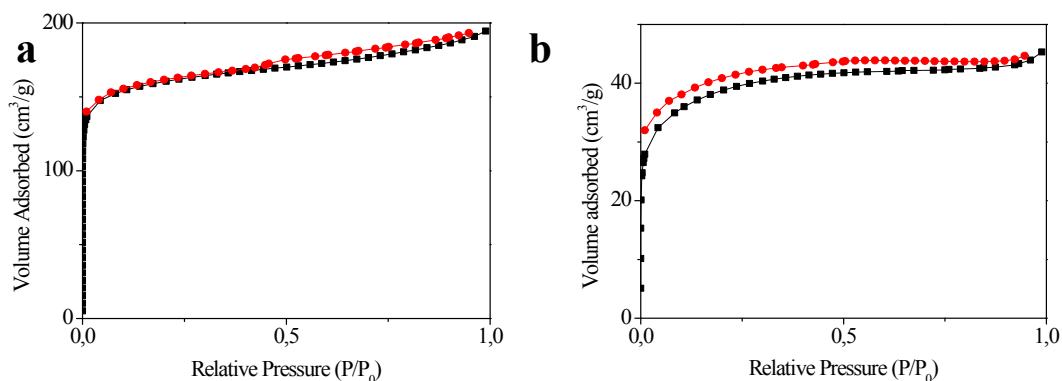


Figure S4. Nitrogen sorption isotherms of (a) Pd@C-HIPE_(25HF) (b) Au@C-HIPE_(25HF).

The nitrogen physisorption isotherms are Type-I, this is to say mainly microporous bearing weak mesoporosity. The micropores are induced by the THF departure when applying the resorcinol resin pre-polymerisation through thermal treatment. Overall these foams specific surface areas expressed with either the BET-or *t*-Plot equations are proposed within the Table S2.

Table S2. Foams mesoscopic characteristics extracted from nitrogen physisorption measurements.

	BET (m ² /g)	<i>t</i> -Plot (m ² /g)
Pd@C-HIPE _(25HF)	606	33
Au@C-HIPE _(25HF)	122	4

When comparing the Pd and Au-based materials we can notice that the overall surface areas are lower when Au nanoparticles are used than in the case of Pd nanoparticles. Indeed, when looking at the HR-TEM microscopy (Figure S7) it appears that the Au nanoparticles are smaller than the Pd ones and more homogeneously dispersed at the macropore surface. This specific feature would minimize nitrogen diffusion through the porosity for the gold loading

foams while maintaining the same skeleton densities for the gold and palladium loading foams.

At the microscopic length scale the first issue to assess is the amount of metal nanoparticles loading within the M@C-HIPE foams. Elemental analyses were performed and gave a value of 8.15 wt% for Pd and 10.07 wt% for Au. The nanoparticles metallic state has been first investigated through XPS experiments, results are proposed within the Figure 5. Typical XPS survey spectra are represented within the Figures 5a and 5b. We can notice that the carbonaceous foams display the presence of carbon and oxygen. The presence of oxygen as heteroatom is expected as we have demonstrated that with the same resorcinol-formaldehyde source of carbon, the deconvolution of the C1s peak in the range 280–295 eV suggests the presence of COOH, COOR, C=O and C-O functions at the walls surface of the foams. Of course, the XPS spectra of the Au/Pd@C-HIPE differ when we focus on the binding energies of Au and Pd. As addressed with the Figure S5d, the Au 4F_{7/2} and 4F_{5/2} peaks present, respectively, at 83.6 and 87.5 eV demonstrate without ambiguity the full reduction of the Au salt into zerovalent metallic nanoparticles.

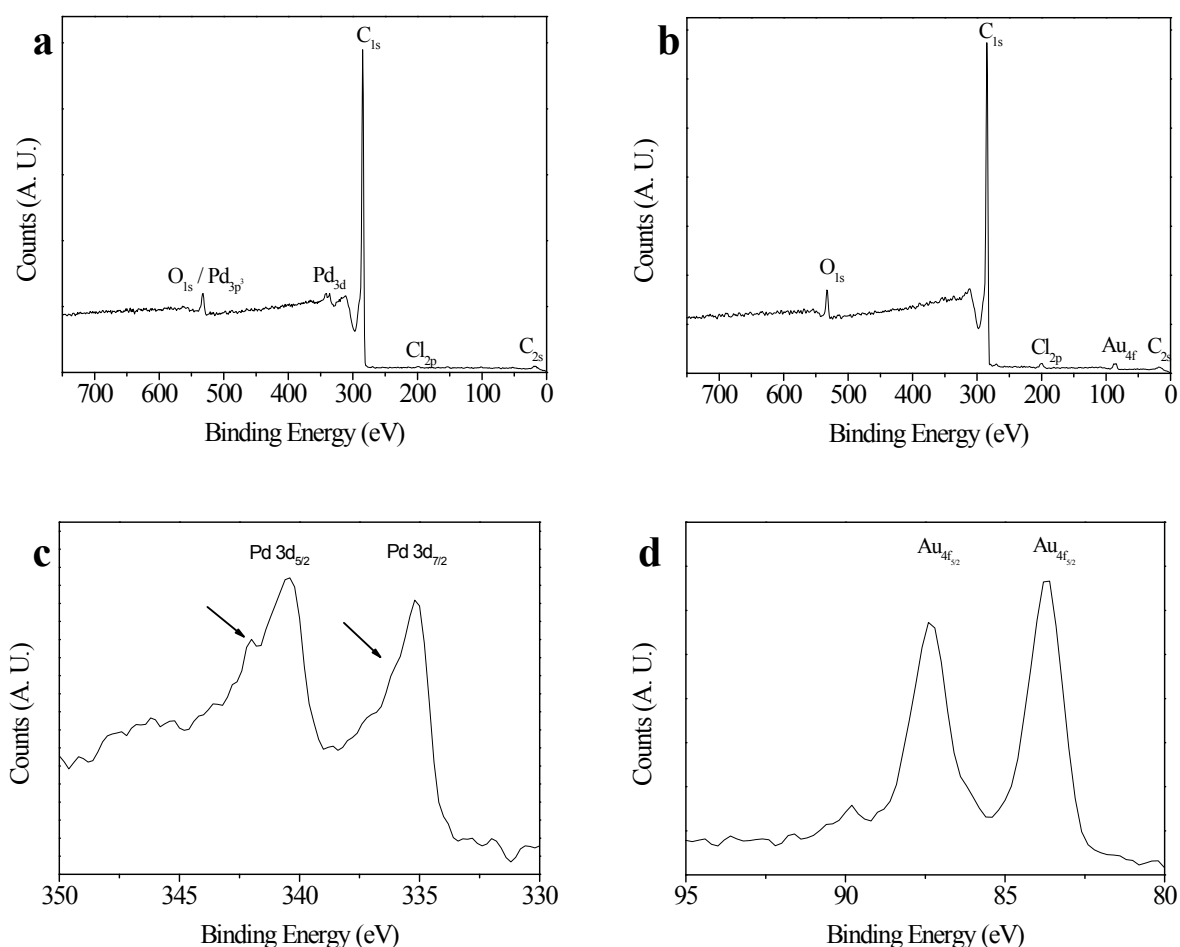


Figure S5. XPS investigations. a) Example of XPS survey acquisition for a Pd@C-HIPE foam, b) example of XPS survey acquisition for a Au@C-HIPE foam, c) XPS spectra of Pd@C-HIPE_(25HF) focused on the Pd binding energy. The black arrows indicate the PdO Pd 3d_{7/2} and Pd 3d_{5/2} peaks. d) XPS spectra of Au@C-HIPE_(25HF) focused on the Au binding energy.

The palladium oxidation state is determined in the Figure S5c. The XPS spectrum shows the Pd 3d_{5/2} and Pd 3d_{7/2} peaks of Pd metallic zerovalent arising respectively at 340.3 eV and 335.5 eV. We can also observe shoulders on both peaks at higher binding energy values which are attributed to palladium oxide (PdO). This feature demonstrates that the Pd⁰ nanoparticles are partially covered with PdO. We have earlier demonstrated that when 1–2 nm of the material surface was dug with an electron beam, we observed a shift of those peaks toward characteristic Pd metallic 3d_{5/2} and 3d_{7/2} peaks. Basically, partial oxidation of Pd nanoparticles surface is always observed when a specific stabilizer as triphenylphosphine or

mercapto groups is not employed. Beyond their zerovalent or oxide nature, the structure of the embedded nanoparticles have been assessed with XRD (Figure S6).

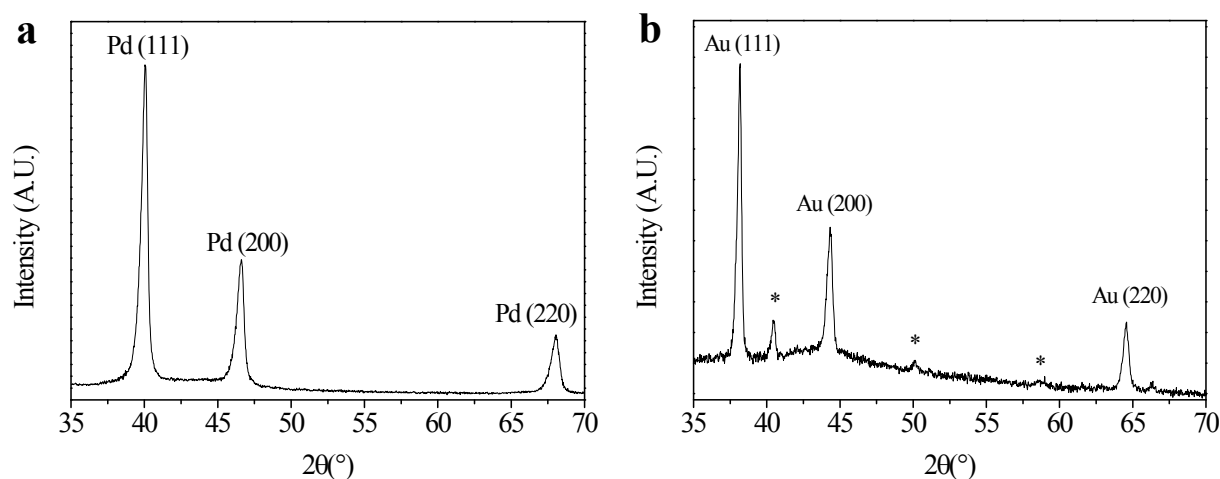


Figure S6. XRD diffractograms (a) Pd@C-HIPE_(25HF) (b) Au@C-HIPE_(25HF). The stars indicate from left to right the KCl (202), (222) and (420) diffraction peaks.

With the Figure S6a, dedicated to the XRD for the Pd-loaded foam, we can notice that the *fcc* three main Bragg diffraction peaks of the Pd nanoparticles are present without ambiguity within the range 35–70° 2θ . There is no evident sign of crystalline palladium oxide species, meaning that the oxidized palladium species are either not highly abundant or small enough not to provide detectable XRD reflections. Considering the Figure 6b we can see that the Au@C-HIPE foam diffraction pattern is bearing, in addition to KCl Bragg peaks formed from KAuCl_4 after the reduction of Au^{3+} , the characteristic Bragg diffractions of metallic *fcc* gold particles in the range 35–70° (2θ). This feature is in agreement with the XPS results considering the zerovalent state of the gold nanoparticles nucleated within these carbonaceous foams.

At that point it was hard to estimate the nanoparticles sizes. To reach this information we have therefore made the use of both TEM and HR-TEM (Figure S7) to directly observe the particles morphology. Considering the Figure S7a,b it is obvious that the nanoparticle sizes distributions are rather polydisperse, both for Pd and Au. From the Figures Sc,d we can

notice that the particles are polycrystalline and grain boundaries can be seen at ease. In order to obtain better quantitative results, we have analyzed several TEM and HR-TEM micrographs to estimate roughly the distribution of particle diameters, results are shown within the Figure S7e,f.

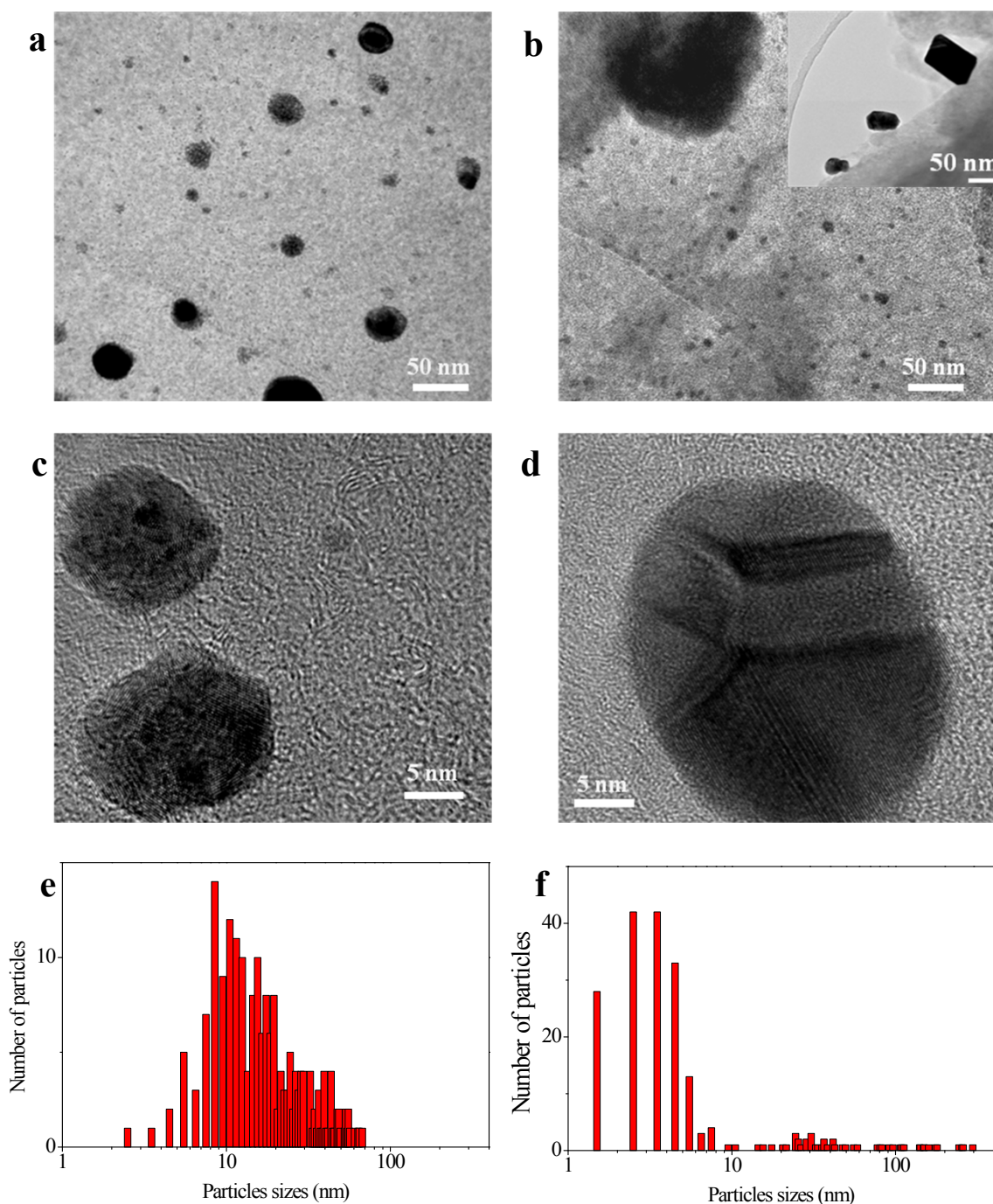


Figure S7. Transmission electron microscopy (a) Pd@C-HIPE_(25HF) (b) Au@C-HIPE_(25HF) (inset HR-TEM on gold nanoparticles anchored at the macroporous surface), (c) Pd@C-HIPE_(25HF) (d) Au@C-HIPE_(25HF) Populations of particle diameters (e) Pd@C-HIPE_(25HF) (f) Au@C-HIPE_(25HF). Populations of

particle diameters were obtained through analyzing both TEM and HR-TEM images. The histograms have been constructed by scanning $2 \mu\text{m}^2$ of each sample.

When considering the particle diameters distribution depicted in Figure 7e,f, we can note that the polydisperse character of the nanoparticle diameters depends on the metal in use. This broad dispersion of particle sizes indicates that we have heterogeneous nucleation distributed both at the micropores and at the macropores surface leading to the higher particle diameters.

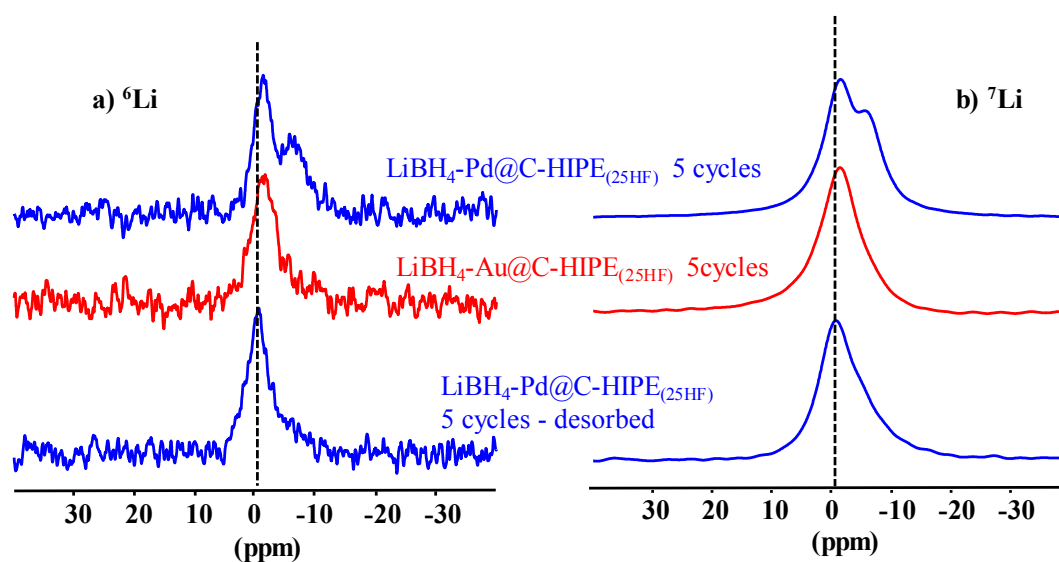


Figure S8. a) ^6Li and b) ^7Li MAS NMR spectra recorded for $\text{LiBH}_4\text{-M@C-HIPE}_{(25\text{HF})}$ after five desorption/absorption cycles and after a sixth desorption for $\text{M} = \text{Pd}$.